ACS NANO

www.acsnano.org

ARTICLE

Self-Assembled *o*-Carborane Clusters Enabling Ambient/Electrochemical Dual-Stable Interphases for Dendrite-Free and High-Rate Lithium Metal Batteries

Yaoda Wang, Junchuan Liang, Tianyu Shen, Xingkai Ma, Zuoxiu Tie, and Zhong Jin*

Cite This: *ACS Nano* 2025, 19, 38760−38772

Read Online

ACCESS | Metrics & More | Article Recommendations | Supporting Information

ABSTRACT: The practical application of lithium (Li) metal batteries is severely hindered by the limited cycling lifespan and worrying safety concerns caused by unstable native solid electrolyte interphase (SEI) and uncontrollable Li dendrite growth. Herein, we report the spontaneous construction of a self-adsorbed *o*-carborane interfacial passivation layer on Li metal anodes via the electrostatic attraction between *o*-carborane molecules and Li metal. The electrochemically stable *o*-carborane clusters can fully participate in the formation of a hybrid SEI, which is endowed with high chemical inertness and structural stability, thus effectively preventing Li metal from electrolyte corrosion. Furthermore, the as-formed *o*-carborane-rich SEI can promote uniform distribution of Li^+ flux and accelerate Li^+ transfer, thereby avoiding dendritic Li formation and enhancing Li plating/stripping reversibility. Consequently, the Li||Li symmetric batteries assembled with *o*-carborane modified Li metal (*o*-carborane/Li) electrodes can cycle stably for over 800 h at 1.0 mA cm^{-2} in carbonate-based electrolytes and 1000 h at 4.0 mA cm^{-2} in ether-based electrolytes. The assembled *o*-carborane/Li||$LiFePO_4$ and *o*-carborane/Li||$LiNi_{0.8}Co_{0.1}Mn_{0.1}O_2$ batteries also achieve exceptional cycling reversibility, prolonged operation lifespan, and superior rate performance. This work offers a promising strategy to develop intriguing self-adsorbed passivation layers for the development of dendrite-free and high-rate Li metal batteries.

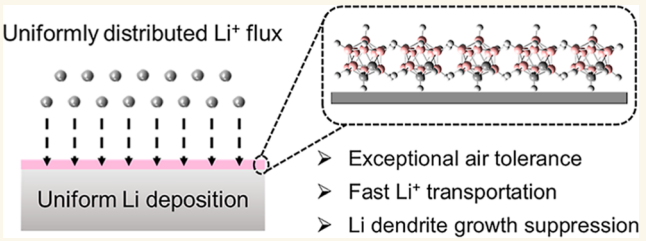

KEYWORDS: *lithium metal anode, o-carborane molecule, self-adsorbed passivation layer, solid electrolyte interphase, lithium dendrite suppression*

Lithium (Li) metal has been considered a promising choice of high-specific-energy anode materials for next-generation energy storage devices.[1−5] However, the deployment of Li metal anodes is greatly hindered by the formation of fragile solid electrolyte interphase (SEI) and uncontrollable Li dendrite growth, which severely threatens the battery safety.[6−11] To eliminate these obstacles, many effective strategies have been proposed, including optimizing electrolyte compositions,[12−14] fabricating 3D porous host materials,[15−17] developing solid-state electrolytes,[18−20] and constructing artificial SEI layers.[21−23] Among the proposed strategies, constructing a well-designed artificial SEI is deemed as a promising option to stabilize Li metal anodes, due to its high controllability and commercial-scale application potential.[24,25] Nevertheless, the constructed SEI usually experiences compositional evolution and structural degradation due to the volume changes of Li metal anodes during long-term cycling, inevitably weakening its protective effect.[26,27] So far, it is still challenging to construct a full-featured artificial SEI that possesses high ionic conductivity for supporting fast Li^+ transfer, chemical inertness for preventing interfacial side reactions, and superior guiding effect for achieving uniform Li electrodeposition.

Carboranes are boron−carbon cluster compounds with polyhedral cage structures, exhibiting high thermal stability, electrochemical inertness, and tunable functionalization for diverse applications.[28] Benefiting from its unique electronic and stereochemical characteristics, *o*-carborane clusters are expected to spontaneously interact with the Li metal electrode to regulate its surface microenvironment. In view of this, here we propose the spontaneous construction of an advanced self-

Received: August 29, 2025
Revised: October 26, 2025
Accepted: October 28, 2025
Published: October 31, 2025

https://doi.org/10.1021/acsnano.5c14816
ACS Nano 2025, 19, 38760−38772

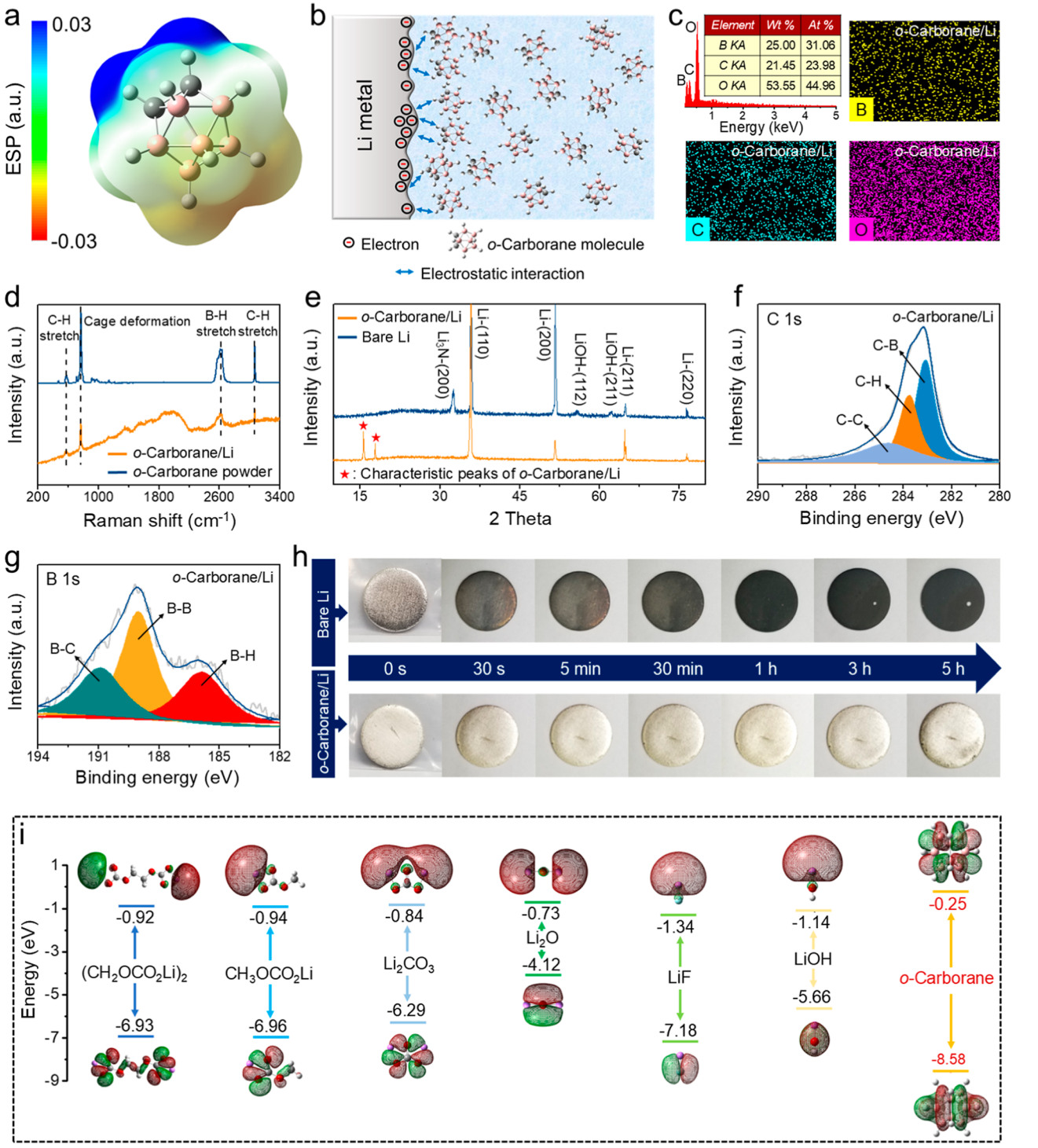

Figure 1. Structural and compositional characterizations of *o*-carborane/Li electrodes and its stability verifications. (a) Simulated ESP mapping of *o*-carborane molecule. (b) Schematic diagram illustrating the formation mechanism of self-adsorbed *o*-carborane passivation layer on Li metal surface via electrostatic interaction. (c) EDX spectrum and corresponding element mappings of *o*-carborane/Li electrodes. (d) Raman spectra of *o*-carborane powder and *o*-carborane/Li electrodes. (e) XRD patterns of bare Li and *o*-carborane/Li electrodes. (f,g) High-resolution XPS spectra at (f) C 1s and (g) B 1s regions of *o*-carborane/Li electrodes. (h) Ambient stability tests of bare Li and *o*-carborane/Li electrodes. Both electrodes were monitored for different durations after exposure to ambient air with a relative humidity of ~60%. (i) Molecular orbital energies of $(CH_2OCO_2Li)_2$, CH_3OCO_2Li, Li_2CO_3, Li_2O, LiF, LiOH and *o*-carborane obtained by DFT calculations.

adsorbed *o*-carborane passivation layer on the Li metal surface. During the initial Li plating process, the self-anchored *o*-carborane molecules fully participate in the formation of a hybrid SEI containing uniformly dispersed *o*-carborane component, providing high electrochemical stability and ionic conductivity. The as-formed hybrid SEI helps guide uniform Li^+ flux and improve the uniformity of Li eletrodeposition, thereby markedly boosting the cycling

https://doi.org/10.1021/acsnano.5c14816
ACS Nano 2025, 19, 38760−38772

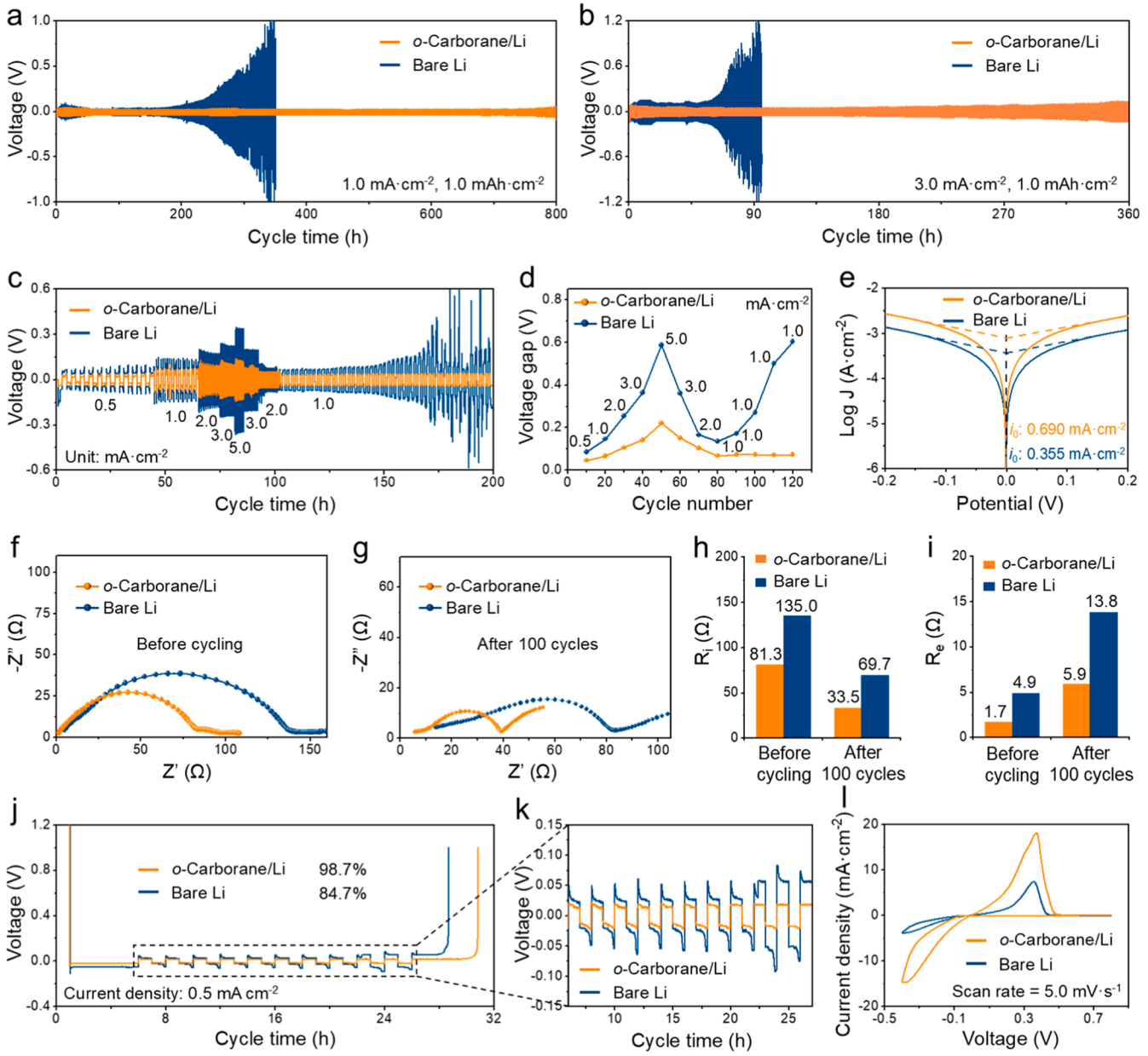

Figure 2. Electrochemical performances of Li||Li symmetric batteries and Li||Cu half batteries assembled with bare Li or *o*-carborane/Li electrodes using conventional carbonate-based electrolytes. (a,b) Galvanostatic cycling stability tests of Li||Li symmetric batteries measured at (a) 1.0 mA cm^{-2} with a capacity of 1.0 mAh cm^{-2} and (b) 3.0 mA cm^{-2} with a capacity of 1.0 mAh cm^{-2}. (c) Rate capability of Li||Li symmetric batteries measured at different current densities from 0.5 mA cm^{-2} to 5.0 mA cm^{-2} with a fixed capacity of 1.0 mAh cm^{-2}. (d) Voltage hysteresis of Li||Li symmetric batteries at different cycles corresponding to Figure 2c. (e) Tafel curves of Li||Li symmetric batteries measured at a scan rate of 5.0 mV s^{-1} from −0.2 to 0.2 V. (f,g) EIS analysis of Li||Li symmetric batteries (f) before and (g) after 100 cycles. (h,i) Comparison of (h) interfacial resistance values and (i) electrolyte resistance values calculated from Figure 2f,g. (j) Voltage−time curves of Li||Cu half batteries measured at 1.0 mA cm^{-2} for calculating the average Coulombic efficiency. (k) Detailed voltage curves of Li plating/stripping on Cu current collectors obtained from Figure 2j. (l) CV curves of Li||Cu half batteries at a scan rate of 5.0 mV s^{-1} from −0.4 to 0.8 V.

stability of batteries. Profiting from these merits, the Li||Li symmetric batteries based on *o*-carborane modified Li metal (*o*-carborane/Li) electrodes exhibit stable Li plating/stripping processes for over 800 h at 1.0 mA cm^{-2} in carbonate-based electrolytes and 1000 h at 4.0 mA cm^{-2} in ether-based electrolytes. When paired with $LiFePO_4$ (LFP) cathodes, the *o*-carborane/Li||LFP batteries achieve a markedly prolonged cycling lifespan for over 1000 cycles with a considerable capacity retention of 75.4% at 5.0 C. The *o*-carborane/Li||$LiNi_{0.8}Co_{0.1}Mn_{0.1}O_2$ (NCM811) batteries also demonstrate superior long-term cycling stability for over 1000 cycles and impressive rate performance of up to 10.0 C. These findings provide new insights for designing self-adsorbed interfacial passivation layers toward stabilizing Li metal anodes, demonstrating a promising solution for the development of next-generation Li metal batteries.

RESULTS AND DISCUSSION

The self-adsorbed *o*-carborane passivation layer was constructed by immersing fresh Li metal electrodes in 0.5 M *o*-

https://doi.org/10.1021/acsnano.5c14816
ACS Nano 2025, 19, 38760−38772

carborane in tetrahydrofuran (THF) solution (Figure S1), which was demonstrated to possess superior dispersion stability and uniformity (Figures S2 and S3). To gain insight into the self-adsorbed behavior of *o*-carborane molecules on Li electrode surface, systematic density functional theory (DFT) calculations were performed. Molecular electrostatic potential (ESP) calculation revealed more notable electro-positivity of hydrogen atoms bonded to carbon atoms in *o*-carborane molecules (Figure 1a), implying the potential electrostatic interactions of C−H bonds with Li metal. The charge distribution of *o*-carborane molecules based on Mulliken populations quantitatively confirmed higher partial positive charges on these hydrogen atoms connected to carbon atoms, further supporting their role as functional sites to interact with Li metal (Figure S4). These findings demonstrated that the spontaneous adsorption phenomenon originated from the unique molecular structure of *o*-carborane. Due to the higher electronegativity of carbon atoms (2.55) compared with boron atoms (2.04), the hydrogen atoms connected to carbon atoms in *o*-carborane molecules have a certain Lewis acidity, which inclines *o*-carborane molecules to strongly anchor on Li metal surface,[28] especially on the protuberant positions with more charge accumulation (Figure 1b). As a result, the self-adsorbed *o*-carborane molecules are expected to guide uniform Li deposition, achieving a smooth and dendrite-free Li plating morphology.

The as-prepared *o*-carborane/Li electrodes presented a flat and uniform surface morphology (Figure S5), and exhibited a white color surface distinct from the bare Li electrodes. The energy dispersive X-ray spectroscopy (EDX) analysis of *o*-carborane/Li electrodes and corresponding elemental mappings showed the uniform distribution of B, C and O elements (Figure 1c), indicating the uniform modification of *o*-carborane molecules. The cross-section morphology of *o*-carborane/Li electrodes was also characterized via scanning electron microscopy (SEM), revealing that the thickness of self-adsorbed *o*-carborane passivation layer was around 600 nm (Figure S6a). Corresponding EDX analysis results verified that the spatial distributions of B and C elements were broadly consistent with the cross-section morphology of as-constructed *o*-carborane interfacial passivation layer (Figure S6b,c), confirming the accuracy of the measured thickness for the *o*-carborane interface passivation layer. The Raman spectrum of *o*-carborane/Li electrodes displayed four characteristic peaks assigned to the C−H stretching, cage deformation, B−H stretching, and C−H stretching of *o*-carborane molecules (Figure 1d),[29,30] verifying the formation of self-adsorbed *o*-carborane protection layer. Distinctive from bare Li electrodes, the characteristic X-ray diffraction (XRD) signals of *o*-carborane were detected on the surface of *o*-carborane/Li electrodes (Figure 1e and S7). The X-ray photoelectron spectroscopy (XPS) analysis of *o*-carborane/Li electrodes clearly exhibited the characteristic peaks of C−C, C−H and C−B species (Figure 1f), and the B−C, B−B and B−H peaks were also detected in the B 1s spectrum (Figure 1g),[31,32] indicating uniformly dispersed *o*-carborane molecules on Li metal surface.

To demonstrate the compactness of self-assembled *o*-carborane passivation layer, the ambient stability of *o*-carborane/Li electrodes was evaluated. After exposed to ambient air atmosphere (Figure 1h), the color of bare Li electrodes completely turned to black within a few minutes. In contrast, no apparent change in color or volume was observed for the *o*-carborane/Li electrodes even after exposure to humid air for 5 h, indicating that the *o*-carborane passivation layer as a physical barrier can effectively prevent gas permeation and stabilize the underneath Li metal in ambient air. Furthermore, the chemical inertness of *o*-carborane passivation layer was investigated by both density functional theory (DFT) calculations and electrochemical tests. Based on Frontier molecular orbital theory, the electrochemical stability of SEI components highly depends on their lowest unoccupied molecular orbital (LUMO) and the highest occupied molecular orbital (HOMO) energies.[33,34] If the LUMO energy of SEI species is lower than the electrochemical potential of Li metal, Li metal will tend to transfer electrons to the unoccupied orbital of the SEI components, thereby triggering their spontaneous decomposition on the Li metal surface. Hence, a desired SEI component should possess a high LUMO energy to enhance the interfacial stability.[33] In this study, the optimized geometries and Frontier molecular orbital energies of conventional SEI components and *o*-carborane molecule were obtained by DFT calculations (Figures 1i, S8 and Table S1). The *o*-carborane demonstrated a much higher LUMO energy (−0.25 eV) than the conventional SEI species formed in carbonate-based electrolytes, such as $(CH_2OCO_2Li)_2$ (−0.92 eV), CH_3OCO_2Li (−0.94 eV), Li_2CO_3 (−0.84 eV), Li_2O (−0.73), LiF (−1.34) and LiOH (−1.14), suggesting that *o*-carborane was a desirable SEI component to stabilize Li metal. Moreover, the electrochemical stability of *o*-carborane passivation layer was also investigated by measuring linear sweep voltammetry (LSV) (Figure S9). Compare with the bare Li electrodes (~4.97 V), the *o*-carborane/Li electrodes exhibited a wider electrochemical stability window (>5.16 V), indicating that the *o*-carborane/Li electrodes possessed valuable potential to match with high-voltage cathodes for the development of high-energy-density Li metal batteries.[35]

To evaluate the reliability of self-assembled *o*-carborane passivation layer and its compatibility with Li metal anodes, the cycling stability of Li||Li symmetric batteries was further investigated at various current densities in both carbonate-based and ether-based electrolytes. At 1.0 mA cm^{-2} with a capacity of 1.0 mAh cm^{-2} (Figure 2a), the Li||Li symmetric batteries with *o*-carborane/Li electrodes exhibited an ultralow overpotential of ~50 mV and outstanding cycling stability for over 800 h in carbonate-based electrolyte (Figure S10a,b), indicating the formation of a stable SEI and fast Li^+ transfer capability. By comparison, unstable voltage profiles with markedly increased voltage hysteresis were observed in the Li||Li symmetric batteries based on bare Li electrodes after cycling for only 200 h. When the current density was increased to 3.0 mA cm^{-2} (Figure 2b), the Li||Li symmetric batteries based on *o*-carborane/Li electrodes could still cycle stably in carbonate-based electrolyte for over 360 h with a low voltage polarization of ~135 mV (Figure S10c,d). However, the Li||Li symmetric batteries with bare Li electrodes exhibited a sharp voltage divergence of about 900 mV after merely 80 h, followed by the battery failure. The cycling stability of Li||Li symmetric batteries measured at a higher capacity of 3.0 mAh cm^{-2} was also investigated in carbonate-based electrolyte (Figure S11). Compared with the significantly increased voltage polarization of bare Li electrodes after 220 h, the *o*-carborane/Li electrodes exhibited highly stable Li plating/stripping behaviors for more than 560 h, confirming the improved interfacial stability and better reaction kinetics. Impressively, the exceptional cycling stability of Li||Li

https://doi.org/10.1021/acsnano.5c14816
ACS Nano 2025, 19, 38760−38772

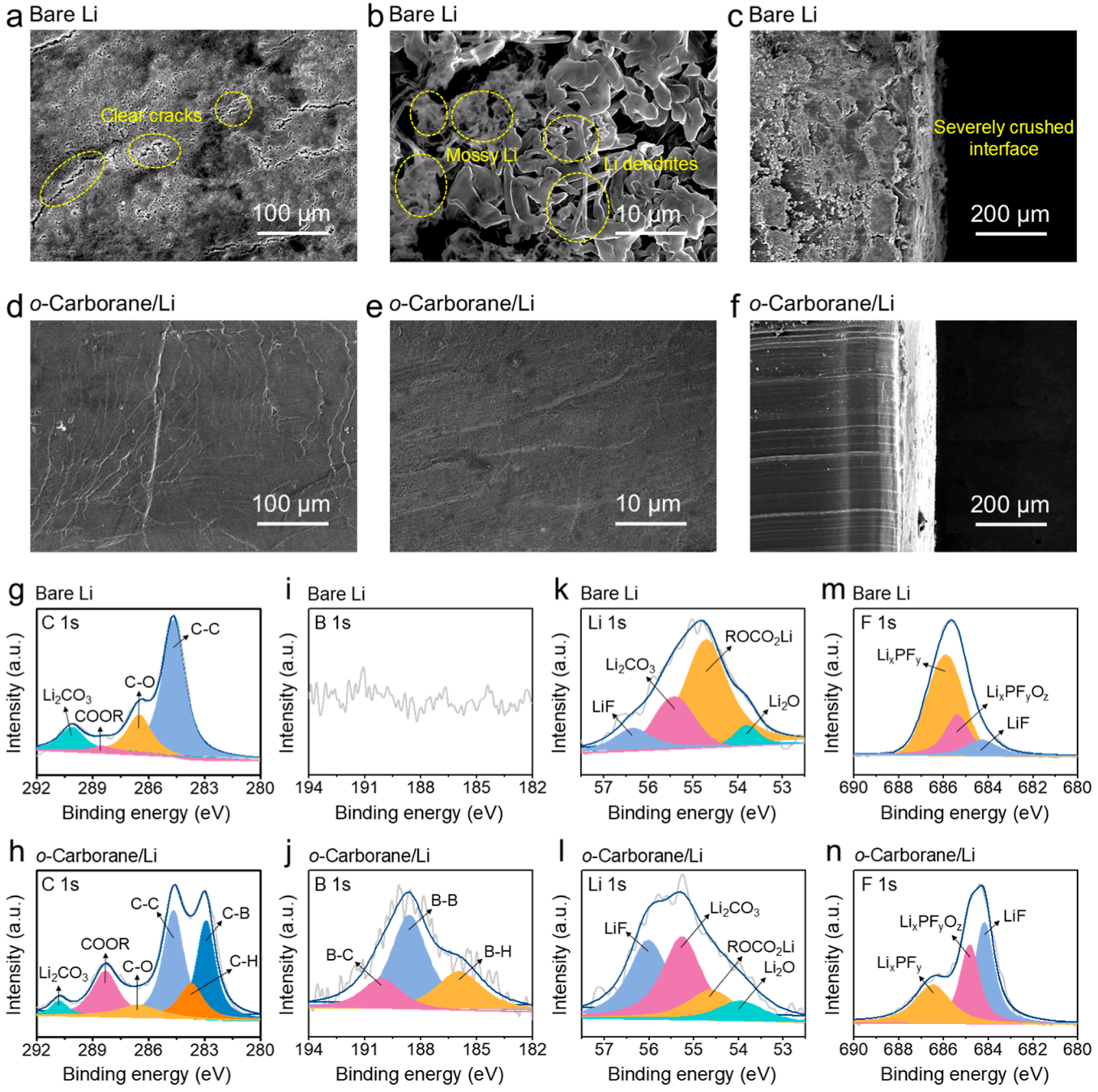

Figure 3. Surface morphology and composition characterizations of bare Li and *o*-carborane/Li electrodes after cycling. (a,b) Top-view and (c) side-view SEM images of bare Li electrodes retrieved from Li||Li symmetric batteries after 100 cycles. (d,e) Top-view and (f) side-view SEM images of *o*-carborane/Li electrodes retrieved from Li||Li symmetric batteries after 100 cycles. High-resolution XPS spectra at (g) C 1s, (i) B 1s, (k) Li 1s, and (m) F 1s regions of bare Li electrodes retrieved from Li||Li symmetric batteries after 50 cycles. High-resolution XPS spectra at (h) C 1s, (j) B 1s, (l) Li 1s, and (n) F 1s regions of *o*-carborane/Li electrodes retrieved from Li||Li symmetric batteries after 50 cycles.

symmetric batteries assembled with *o*-carborane/Li electrodes is highly competitive compared to those of previously reported Li electrodes stabilized by different artificial SEI layers (Table S2),[8,24,36−45] further highlighting the superiority of as-constructed *o*-carborane interfacial passivation layer in stabilizing Li metal electrodes.

The rate performance of Li||Li symmetric batteries was also measured at different current densities in carbonate-based electrolyte (Figure 2c). When assembled with bare Li electrodes, the Li||Li symmetric batteries exhibited significantly increased voltage polarization from 43 to 294 mV as the current densities increased from 0.5 to 5.0 mA cm^{-2} (Figure 2d). By comparison, the Li||Li symmetric batteries based on *o*-carborane/Li electrodes maintained stable voltage curves with low overpotentials increasing from 23 to 110 mV. The enhanced rate performance of *o*-carborane/Li electrodes further verified the *o*-carborane-rich SEI possessed high Li^+ conductivity and electrochemical stability. In addition, the significant differences of Li||Li symmetric batteries in cycling stability were also demonstrated when using ether-based

https://doi.org/10.1021/acsnano.5c14816
ACS Nano 2025, 19, 38760−38772

electrolyte (Figure S12). The Li||Li symmetric batteries with *o*-carborane/Li electrodes displayed highly improved cyclability and limited voltage hysteresis at various current densities and capacities. In contrast, the Li||Li symmetric batteries based on bare Li electrodes suffered from increased voltage polarization, remarkable voltage fluctuations and sudden battery failure under the same current densities and capacities, further highlighting the superiority of *o*-carborane passivation layer in improving Li plating/stripping stability.

To verify the improved electrochemical kinetics of *o*-carborane/Li electrodes, the exchange current density (i_0) was calculated from the Tafel plots of Li||Li symmetric batteries (Figure 2e). The i_0 value of *o*-carborane/Li electrodes was as high as 0.690 mA cm^{-2}, much higher than that of bare Li electrodes (0.355 mA cm^{-2}), indicating that the interfaces between the electrolyte and *o*-carborane/Li electrode supported rapider Li^+ transport.[46] Electrochemical impedance spectroscopy (EIS) analysis was also conducted to reveal the variation of interfacial resistances and electrolyte resistances in Li||Li symmetric batteries before and after 100 cycles (Figure 2f,g). It is generally accepted that the intercept of the high-frequency response with the real axis is an indication of the electrolyte resistance (R_e), while the intermediate-to-high-frequency semicircle mainly represents the interfacial resistance (R_i) at the electrode/electrolyte interface.[47] Before cycling, the interfacial resistance of *o*-carborane/Li electrodes was 81.3 Ω, which significantly reduced to 33.5 Ω after 100 repeated Li plating/stripping cycles, indicating the formation of a stable hybrid SEI with rapid Li^+ transfer kinetics. By comparison, the interfacial resistances of bare Li electrodes reached 135.0 and 69.7 Ω before and after 100 cycles, respectively (Figure 2h). Regarding the electrolyte resistance, the *o*-carborane/Li electrodes exhibited a slight increase from 1.7 to 4.9 Ω after 100 cycles. Whereas for bare Li electrode, the electrolyte resistance sharply increased from 5.9 to 13.8 Ω (Figure 2i), illustrating that the fragile native SEI on bare Li electrode could hardly avoid electrolyte consumption and Li metal corrosion during cycling.

To testify the effect of self-adsorbed *o*-carborane passivation layer in boosting Li plating/stripping reversibility, the electrochemical performances of Li||Cu half batteries were tested and compared. The average Coulombic efficiency of the Li||Cu half batteries based on *o*-carborane/Li electrodes was up to 98.7% during 10 Li plating/stripping cycles (Figure 2j). By comparison, the Li||Cu half batteries with bare Li electrodes only delivered an average Coulombic efficiency of 84.7%. The detailed voltage curves of Li plating/stripping on Cu current collectors were also compared. The Li||Cu half batteries assembled with *o*-carborane/Li electrodes exhibited well-maintained overpotentials, much lower than those of bare Li electrodes (Figure 2k). Cyclic voltammetry (CV) measurements of Li||Cu half batteries were performed, showing the much higher current responses of *o*-carborane/Li||Cu half batteries than those of bare Li||Cu half batteries (Figure 2l), corresponding to rapid Li^+ transport and highly reversible reaction kinetics of *o*-carborane/Li electrodes.[48,49] Moreover, to evaluate the long-term cycling reversibility of *o*-carborane/Li electrodes, the prolonged Li plating/stripping processes of Li||Cu half batteries were investigated (Figure S13). When using *o*-carborane/Li electrodes, the batteries displayed markedly improved cycling stability, achieving a well-maintained CE of 98.84% after 300 cycles. In comparison, limited cycling lifespans and significant CE fluctuations were observed for the bare Li||Cu half batteries, highlighting the key role of *o*-carborane interfacial passivation layer in boosting cycling reversibility and stability of Li metal electrodes.

To intuitively illustrate the guidance effect of *o*-carborane passivation layer on homogeneous Li deposition, the real-time morphology variations of bare Li and *o*-carborane/Li electrodes during Li plating/stripping processes were monitored in a symmetric sealed transparent battery. For bare Li electrodes (Figure S14a), the initial smooth and flat surface was covered by sharp Li dendrites after only 30 cycles, presenting a rough and uneven interface morphology. As the Li plating/stripping process continued, the nonuniformity of Li deposition was further aggravated. Finally, the bare Li electrode surface was fully covered by dendritic and dead Li after 120 cycles. In sharp contrast, steady Li plating/stripping behavior was achieved when using *o*-carborane/Li electrodes (Figure S14b). Throughout cycling, the smooth and dense electrode surface was well maintained without any visible dendritic and mossy Li, fully demonstrating that the *o*-carborane passivation layer could efficiently guide uniform Li deposition and boost interfacial stability.

To further reveal the distinct differences in surface microstructure of cycled bare Li and *o*-carborane/Li electrodes, SEM technique was utilized to investigate their surface morphologies after 100 cycles. For the bare Li electrodes, a coarse and porous surface with clear cracks was observed (Figure 3a). The magnified SEM image displayed that the bare Li electrode surface after cycling had been completely covered by sharp Li dendrites and symbiotic mossy Li (Figure 3b). Evidently, the bare Li electrodes suffered from the severe electrolyte corrosion and the structure of native SEI was completely destroyed after 100 cycles. The side-view morphology of bare Li electrodes further confirmed the above conclusion, presenting an uneven and rough surface with severe pulverization (Figure 3c). On the contrary, the cycled *o*-carborane/Li electrodes showed a flat and dense surface without any visible microcracks and Li dendrite nucleation (Figure 3d,e), and the side-view morphology of *o*-carborane/Li electrodes was also smooth and compact (Figure 3f), illustrating that the *o*-carborane-rich SEI possessed sufficient structural and electrochemical stability to effectively prevent Li dendrite growth and ensure high-efficient Li plating/stripping behaviors.

The surface chemical composition differences of cycled bare Li and *o*-carborane/Li electrodes were investigated by comprehensive spectroscopic characterizations. The EDX spectrum and corresponding elemental mappings of *o*-carborane/Li electrodes after cycling showed the uniform distribution of B, C, O and F elements (Figure S15), indicating the high durability of *o*-carborane-rich SEI. Four typical characteristic peaks of C−H stretching, cage deformation, B−H stretching, and C−H stretching were also detected in the Raman spectrum of the *o*-carborane/Li electrodes after cycling (Figure S16), confirming the exceptional structural and electrochemical stability of *o*-carborane-rich SEI. XPS characterization was conducted to further identify the SEI composition differences of cycled bare Li and *o*-carborane/Li electrodes. In the C 1s XPS spectrum, four typical peaks were detected on the bare Li electrode surface at 290.1, 288.5, 286.5, and 284.7 eV, corresponding to Li_2CO_3, COOR, C−O, and C−C species, respectively (Figure 3g). By comparison, two additional peaks assigned to C−B (283.7 eV) and C−H (282.9 eV) were detected on the *o*-carborane/Li electrode surface

https://doi.org/10.1021/acsnano.5c14816
ACS Nano 2025, 19, 38760−38772

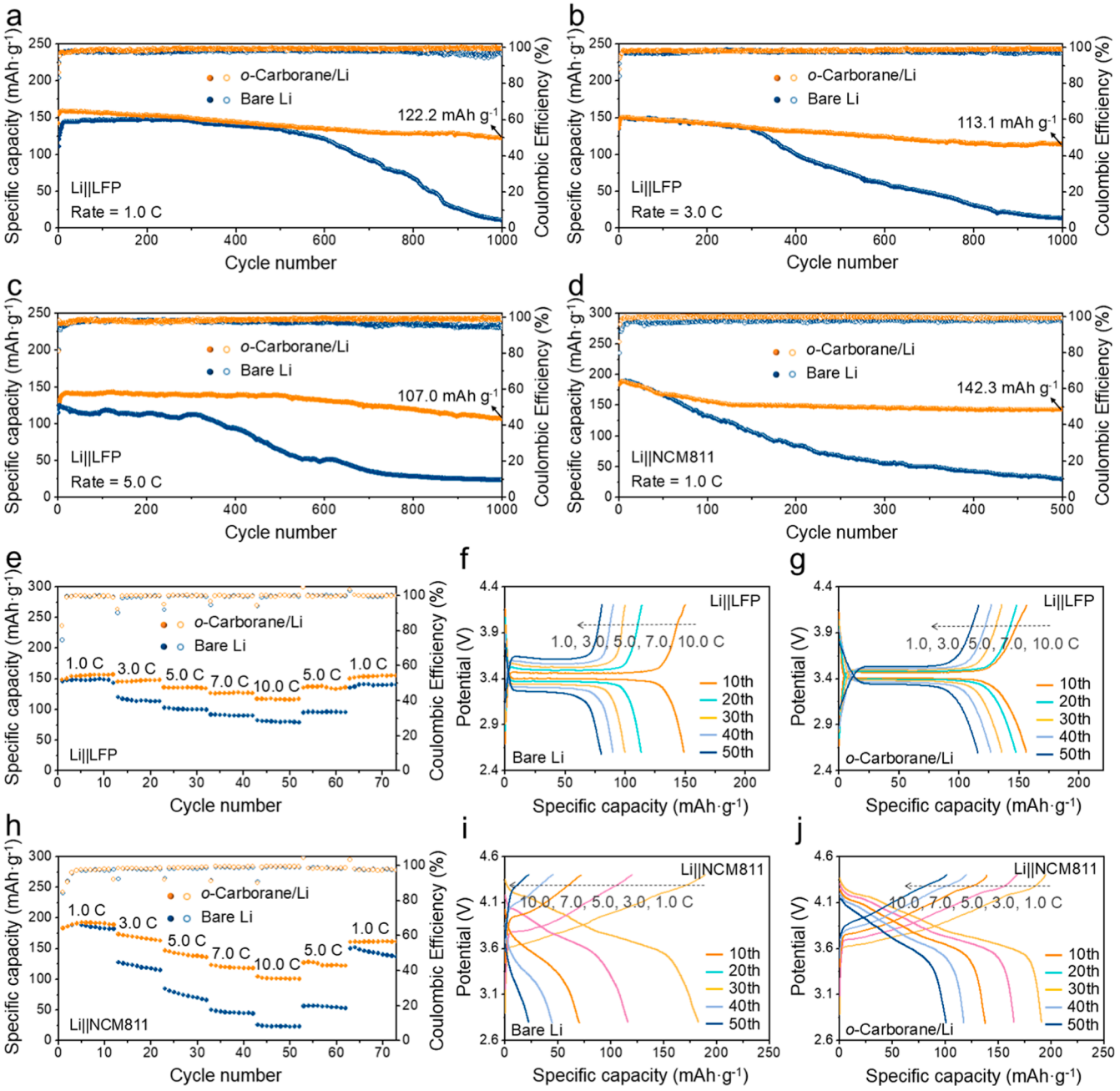

Figure 4. Electrochemical performances of Li||LFP and Li||NCM811 batteries assembled with bare Li and *o*-carborane/Li anodes. (a–c) Cycling performances of Li||LFP batteries tested at (a) 1.0 C (1.0 C = 170 mA g^{-1}), (b) 3.0 C, and (c) 5.0 C. (d) Cycling performances of Li||NCM811 batteries tested at 1.0 C (1.0 C = 200 mA g^{-1}). (e) Rate performances of Li||LFP batteries tested at various current rates from 1.0 to 10.0 C. (f,g) Galvanostatic charge/discharge profiles of Li||LFP batteries assembled with (f) bare Li and (g) *o*-carborane/Li anodes at various current rates. (h) Rate performance of Li||NCM811 batteries measured at various current rates from 1.0 to 10.0 C. (i,j) Galvanostatic charge/discharge profiles of Li||NCM811 batteries assembled with (i) bare Li and (j) *o*-carborane/Li anodes at various current rates.

(Figure 3h), demonstrating the high structural stability of *o*-carborane clusters and their full participation in the formation of hybrid SEI. This conclusion was further verified by the B 1s XPS spectra. Compared with the bare Li electrode with an absence of boronic species (Figure 3i), the B 1s XPS spectrum of *o*-carborane/Li electrodes displayed three typical peaks of B–C, B–B, and B–H species at 190.1, 188.6, and 185.9 eV, respectively (Figure 3j). In addition, four typical signal peaks of LiF, $ROCO_2Li$, Li_2CO_3, and Li_2O were detected at 56.7, 55.4, 54.7, and 53.8 eV, respectively, in the Li 1s XPS spectra of both electrodes (Figure 3k,l). However, larger peak areas of LiF, Li_2CO_3, and Li_2O species were observed for the *o*-carborane/Li electrodes, illustrating the distinct chemical compositions in the *o*-carborane-rich SEI. The results of F 1s and O 1s XPS spectra also supported the above conclusion (Figures 3m,n and S17), illustrating the *o*-carborane-rich SEI was essentially a stable hybrid interfacial layer rich in *o*-carborane, LiF and other inorganic lithiated species, which could effectively protect Li metal from electrolyte attack, promote uniform Li deposition, and accelerate Li^+ transfer. To further investigate the variation of SEI compositions with detection depth, we conducted the in-depth XPS analyses for the cycled *o*-carborane/Li electrodes

https://doi.org/10.1021/acsnano.5c14816
ACS Nano 2025, 19, 38760–38772

by Ar^+ sputtering for 1 and 3 min (Figure S18). The test results demonstrated that the SEI derived on *o*-carborane/Li anodes was a hybrid interphase composed of *o*-carborane components along with other inorganic and organic species. This SEI exhibited no obvious differences in chemical compositions and relative contents of constituent species between its surface and bulk regions. The detected *o*-carborane components distributed throughout the bulk phase of the SEI, rather than being confined solely to the surface. It was confirmed that the *o*-carborane-derived SEI possessed relatively uniform chemical compositions and high electrochemical stability, contributing to the sustained protection for Li metal anodes during long-term cycling processes. Benefiting from its optimized protective interphase, the retrieved *o*-carborane/Li electrodes after long-term cycling could still maintain impressive ambient stability, presenting a flat surface with metallic luster even if exposed to air atmosphere for over 3 h (Figure S19).

To further examine the feasibility and practicality of *o*-carborane/Li anodes, the Li||LFP and Li||NCM811 batteries were assembled and tested. When cycled at 1.0 C, the Li||LFP batteries assembled with *o*-carborane/Li anodes exhibited highly superior cycling stability (Figure 4a), delivering a reversible discharge capacity of 122.2 mAh g^{-1} with a high capacity retention of 76.3% after 1000 cycles, while the Li||LFP batteries based on bare Li anodes suffered from fast capacity decay and significant deterioration in reversibility, delivering a low discharge capacity of 11.0 mAh g^{-1} and a decreased CE of 94.9% after 1000 cycles. When the current rate was increased to 3.0 C (Figure 4b), the Li||LFP batteries based on *o*-carborane/Li anodes could still maintain exceptional cycling stability and high Li utilization for over 1000 cycles, delivering a considerable specific discharge capacity of 113.1 mAh g^{-1} (corresponding to a capacity retention of 74.0%). In contrast, for the Li||LFP batteries assembled with bare Li anodes, a significant capacity attenuation occurred after only 300 cycles. The specific discharge capacity was as low as 13.7 mAh g^{-1} after 1000 cycles, corresponding to a capacity retention of only 9.1%. The distinct differences of Li||LFP batteries in cycling performance were further highlighted at a higher current rate of 5.0 C (Figure 4c). When assembled with *o*-carborane/Li anodes, the Li||LFP batteries achieved a high capacity retention of 75.4% and considerable CE of 98.8% after 1000 cycles. In contrast, the Li||LFP batteries based on bare Li anodes demonstrated sharp capacity deterioration and decreased cycling reversibility, illustrating that the unstable bare Li/electrolyte interface severely aggravated the side reactions and the batteries were close to failure. To further demonstrate the potential of *o*-carborane/Li anodes in developing high-specific-energy Li metal batteries, the Li||LFP batteries based on high-loading LFP cathodes (~2.4 mAh cm^{-2}) were assembled and tested. When assembled with bare Li anodes, the high-loading Li||LFP batteries exhibited continual capacity attenuation, and the specific discharge capacity significantly decreased to 54.5 mAh g^{-1} after only 180 cycles (Figure S20). In contrast, when upgrading to *o*-carborane/Li anodes, the high-loading Li||LFP batteries displayed exceptional cycling stability, achieving a marked prolonged cycling lifespan of 300 cycles with a considerable remaining capacity of 130.7 mAh g^{-1}. The prominent differences in cycling performances of high-loading Li||LFP batteries confirmed the great potential of *o*-carborane interfacial passivation layer in boosting the durability of Li metal batteries.

To further confirm high air tolerance and interfacial stability of *o*-carborane/Li anodes, both bare Li and *o*-carborane/Li anodes were reassembled into Li||LFP batteries after being exposed to ambient air for 30 min. Prior to air exposure, these Li metal anodes had already worked for 100 cycles in Li||LFP batteries. As shown in Figure S21, the batteries based on bare Li anodes barely functioned, exhibiting clearly degraded specific discharge capacity and Coulombic efficiency from the initial cycles, which indicated that the air-exposed bare Li anodes could no longer maintain stable Li plating/stripping processes due to their composition degradation. By comparison, the batteries based on *o*-carborane/Li anodes could still cycle stably, achieving high cycling reversibility and considerable capacity retention. The results further indicated that the constructed *o*-carborane interfacial passivation layer could endow Li metal anodes with high interfacial stability, ensuring a prolonged stable Li plating/stripping process. Moreover, the long-term cycling performances of Li||NCM811 batteries were also tested to further highlight the advantage of *o*-carborane/Li anodes. As displayed in Figure 4d, the Li||NCM811 batteries based on *o*-carborane/Li anodes presented a markedly prolonged cycling lifespan of over 500 cycles at 1.0C, delivering a specific discharge capacity of 142.3 mAh g^{-1} (corresponding to a capacity retention of 75.6%). In contrary, continuous capacity attenuation and fluctuating CE were observed for the Li||NCM811 batteries based on bare Li anodes, and the specific discharge capacity was only 19.8 mAh g^{-1} after 500 cycles, indicating the poor compatibility of bare Li anodes with carbonate-based electrolytes.

The rate performances of Li||LFP and Li||NCM811 batteries were also studied using different anodes at various current rates. For the Li||LFP batteries assembled with bare Li anodes, the reversible discharge capacity was up to 148.8 mAh g^{-1} at 1.0 C (Figure 4e), but sharply dropped to only 79.5 mAh g^{-1} at 10.0 C, which was mainly due to the sluggish reaction kinetics of bare Li anodes. By comparison, the Li||LFP batteries based on *o*-carborane/Li anodes exhibited well-maintained specific discharge capacities of 156.1, 146.3, 135.5, 126.6, and 116.5 mAh g^{-1} at the current rates of 1.0, 3.0, 5.0, 7.0, and 10.0 C, respectively, highlighting the superiority of *o*-carborane/Li anodes in fast charge/discharge. The better rate performance of the *o*-carborane/Li anodes should be ascribed to its lower polarization and faster reaction kinetics, which was confirmed by the smaller potential differences between charge/discharge plateaus at various current rates of *o*-carborane/Li anodes (Figures 4f,g and S22a). The Li||NCM811 batteries assembled with *o*-carborane/Li anodes also demonstrated the significantly boosted rate capability (Figure 4h). For the bare Li||NCM811 batteries, the specific discharge capacities decreased markedly with the increase of current rates. Especially when cycled at 10.0 C, the batteries only delivered a specific discharge capacity of 23.5 mAh g^{-1}. In contrast, the Li||NCM811 batteries based on *o*-carborane/Li anodes maintained considerable capacity retentions, delivering reversible discharge capacities of 191.5, 166.4, 140.8, 118.8, and 101.2 mAh g^{-1} at 1.0, 3.0, 5.0, 7.0, and 10.0 C, respectively. By further examining the charge/discharge voltage curves of Li||NCM811 batteries, it was found that the batteries assembled with *o*-carborane/Li anodes exhibited much lower voltage polarization especially at high current rates (Figures 4i,j and S22b), further corroborating the improved interfacial stability and mass-transfer kinetics of *o*-carborane/Li anodes.

https://doi.org/10.1021/acsnano.5c14816
ACS Nano 2025, 19, 38760−38772

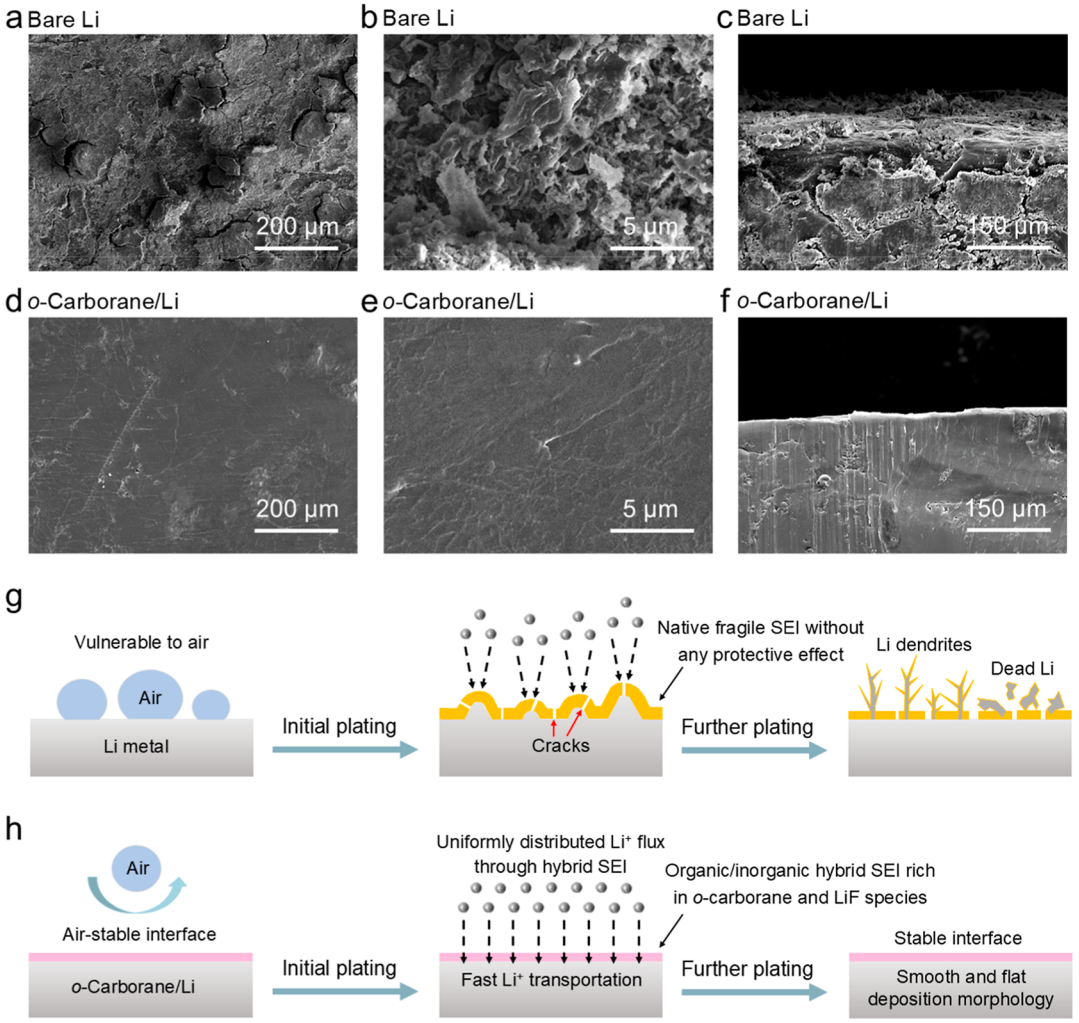

Figure 5. Surface morphologies of cycled bare Li and *o*-carborane/Li anodes in Li||LFP batteries and protection mechanism of self-adsorbed *o*-carborane passivation interphases. (a,b) Top-view and (c) side-view SEM images of the bare Li anodes retrieved from Li||LFP batteries after 200 cycles at 2.0 C. (d,e) Top-view and (f) side-view SEM images of *o*-carborane/Li anodes retrieved from Li||LFP batteries after 200 cycles at 2.0 C. (g,h) Schematic illustrations of Li electroplating behaviors for (g) bare Li and (h) *o*-carborane/Li anodes.

The investigations on practical *o*-carborane/Li||LFP and *o*-carborane/Li||NCM811 batteries demonstrated their significantly prolonged cycling lifespan and improved cycling reversibility. To explore the reasons for battery performance improvement, SEM characterizations were carried out to investigate the surface morphologies of anodes and cathodes retrieved from Li||LFP batteries after 200 cycles. On the anodic side, the cycled bare Li anodes displayed a loose and porous surface morphology with severe pulverization (Figure 5a). A further magnified SEM image (Figure 5b) showed that the bare Li anode surface was completely covered by mossy Li and exfoliated dead Li, which greatly hindered the Li^+ transport through the SEI and seriously deteriorated the electrochemical stability of the Li metal anodes. The side-view SEM image of bare Li anodes also exhibited a rough and cracked surface morphology (Figure 5c), indicating that the fragile native SEI could hardly protect bare Li from the electrolyte attack. In sharp contrast, the cycled *o*-carborane/Li anodes maintained a smooth and dense surface morphology throughout the cycling processes without any visible Li dendrites (Figure 5d–f), confirming the crucial role of as-constructed *o*-carborane interfacial passivation layer in guiding uniform Li deposition and suppressing Li dendrite growth. Due to the unique molecular structure, the *o*-carborane clusters tended to preferentially adsorb onto the protrusions of the Li metal anodes, thereby alleviating the issue of nonuniform Li deposition caused by the tip effect. Furthermore, the self-anchored *o*-carborane clusters were demonstrated to fully participate in the formation of SEI on the *o*-carborane/Li anodes. This incorporation endowed the resulting SEI with high Li^+ transport capabilities, thereby effectively mitigating the nonuniformity of Li^+-flux distribution at the electrode/electrolyte interface and avoiding uneven Li deposition. Collectively, the above factors ensured that the *o*-carborane/Li anodes maintained a flat and smooth surface morphology even after more than 200 cycles. Additionally, it is essential to clarify that the Li deposition processes occurred beneath the *in situ* formed *o*-carborane-derived SEI. During the cycling processes, the preconstructed *o*-carborane interfacial passivation layer was reconstituted into a new SEI, where the *o*-carborane component coexisted with other inorganic and organic species. Consequently, after long-term cycling, the *in situ* formed *o*-carborane-derived SEI did not exhibit a clearly defined boundary distinct with the Li metal substrate, as shown in the enlarged side-view SEM images (Figure S23).

https://doi.org/10.1021/acsnano.5c14816
ACS Nano 2025, 19, 38760–38772

The differences in surface morphologies of the cycled LFP cathodes were also studied and compared by SEM characterizations. When paired with the bare Li anodes (Figure S24a,b), the cycled LFP cathodes displayed clearly damaged surface morphology with the exacerbated grain fusion after 200 cycles, which implied extremely slow reaction kinetics of LFP cathodes in the bare Li||LFP batteries. When paired with the *o*-carborane/Li anode, the surface morphology of the cycled LFP cathode was improved significantly (Figure S24c,d), presenting a desired granular morphology similar to that of pristine LFP cathodes (Figure S24e,f), indicating the achievement of highly efficient Li^+ intercalation/deintercalation of LFP cathodes. EDX analysis results also supported the above conclusion. Compared with the LFP cathodes paired with bare Li anodes (Figure S25), the LFP cathodes paired with *o*-carborane/Li anodes were detected to have almost no loss of Fe and P element contents (Figures S26 and S27), which illustrated the smooth Li^+ transfer ensured the compositional stability and structural integrity of LFP cathodes. It is well accepted that the enhanced Li plating/stripping kinetics of Li metal anodes will effectively promote Li^+ intercalation/deintercalation kinetics of cathode materials.[50] Therefore, it is inferred that the outstanding chemical and structural stability of LFP cathodes in the *o*-carborane/Li||LFP batteries was closely related to the rapid Li^+ transport of *o*-carborane/Li anodes, further demonstrating the superiority of the constructed self-adsorbed *o*-carborane passivation interphases.

Figure 5g,h further schematically illustrated the distinct Li electroplating behaviors of bare Li and *o*-carborane/Li anodes. During the initial Li deposition process, the bare Li anodes tended to form a fragile native SEI and underwent nonuniform Li nucleation and growth due to tip effects and inhomogeneous Li^+ concentration gradients. As the Li plating/stripping process continued, the nonuniformity of Li deposition further intensified, leading to the repeated rupture and reconstruction of native SEI, uncontrollable Li dendrite growth, numerous dead Li proliferation. By comparison, the *o*-carborane/Li anodes could form a robust and stable *o*-carborane-rich SEI, thus achieving uniform Li nucleation in the initial cycling process. Benefiting from the abundant *o*-carborane and other inorganic lithiated species, the as-formed *o*-carborane hybrid SEI could simultaneously achieve rapid Li^+ transfer and long-lasting interfacial stability, ensuring that the *o*-carborane/Li anodes maintained a smooth surface morphology throughout the long-term cycling.

CONCLUSION

In summary, here we report the construction of a self-adsorbed *o*-carborane cluster passivation interphase with high ambient durability and superior electrochemical stability on Li metal anode surface based on the electrostatic attraction between *o*-carborane molecules and Li metal. The self-anchored *o*-carborane clusters fully participated in the SEI formation during the initial Li plating process, and endowed the as-formed hybrid SEI with impressive chemical inertness and high Li^+ conductivity. Therefore, the fabricated *o*-carborane/Li electrodes exhibited boosted electrolyte compatibility, impressive interfacial stability and accelerated mass-transfer kinetics, efficiently facilitating uniform Li electrodeposition and inhibiting Li dendrite growth. Benefiting from these merits, the assembled Li||Li symmetric batteries with the *o*-carborane/Li electrodes achieved markedly prolonged cycling lifespans with the limited voltage polarization in both carbonate-based electrolytes and ether-based electrolytes. Even cycled at a high current rate of 5.0 C, the Li||LFP batteries based on *o*-carborane/Li anodes still exhibited outstanding cycling stability and reversibility. When paired with high-voltage NCM811 cathodes, the *o*-carborane/Li anodes also enabled Li||NCM811 batteries to work stably, achieving excellent cyclability, exceptional rate capability, and markedly improved reaction kinetics. These findings provide new insights for designing a highly durable interfacial passivation layer toward stabilizing Li metal anodes, demonstrating a feasible solution for promoting the development of high-safety lithium metal batteries.

EXPERIMENTAL SECTION

Preparation of *o*-Carborane-modified Li Metal (*o*-Carborane/Li) Anodes. The *o*-carborane/Li anodes were prepared by a typical solution soaking method. Specifically, Li foils (with the diameter of 12 mm and the thickness of 400 μm) were polished using plastic scraper in an argon-filled glovebox with H_2O and O_2 levels <0.1 ppm. The fresh Li foils were polished to remove possible oxidization layers and contaminations, and then immersed in a 1.0 mL tetrahydrofuran (THF) solution containing 0.5 M *o*-carborane for 5 min. After drying at room temperature for about 10 min to evaporate the solvent completely, the *o*-carborane/Li anodes with white surface were obtained and preserved in the glovebox prior to use.

Preparation of $LiFePO_4$ (LFP) and $LiNi_{0.8}Co_{0.1}Mn_{0.1}O_2$ (NCM811) Cathodes. Typically, 80 wt % of LFP powder, 10 wt % of carbon black (super P), and 10 wt % of polyvinylidene fluoride (PVDF) were mixed in *N*-methyl-2-pyrrolidone (NMP) to form a homogeneous slurry. After magnetic stirring for 12 h, the slurry was uniformly spread onto a piece of Al foil by blade coating and dried under vacuum at 100 °C overnight. The as-obtained electrodes were cut into small disks with a diameter of 14 mm. The areal active material loading of LFP cathodes was normally 5.0−5.5 mg cm^{-2} (~0.9 mAh cm^{-2}), and was further increased to 14.0−14.2 mg cm^{-2} (~2.4 mAh cm^{-2}) for the battery tests with high loading cathodes. The NCM811 cathodes were prepared in the same way, and the areal active material loading of NCM811 cathodes was 5.6−6.2 mg cm^{-2} (~1.2 mAh cm^{-2}).

Material Characterizations. The morphology of samples was characterized by field-emission scanning electron microscope (FESEM, FEI Nova-450 V) coupled with an attached energy dispersive X-ray spectroscopy apparatus (EDX, Bruker Quantax-200). Powder X-ray diffraction (XRD) analysis was performed on a Shimadzu 6000 X-ray diffractometer equipped with a Cu Kα radiation (λ = 1.54178 Å). Attenuated total reflectance Fourier transform infrared (ATR-FTIR) spectra were measured on a Nicolet iS50 spectrometer. Raman spectra were acquired by a Horiba LabRAM Evolution Raman spectrometer with an excitation laser of 473 nm wavelength. X-ray photoelectron spectroscopy (XPS) was performed on a PHI-5000 VersaProbe spectrometer using an Al Kα radiation source. The binding energy values were calibrated using the C−C peak in the C 1s spectrum at 284.6 eV. Operando optical microscopy observation was performed on a homemade transparent pouch battery. Optical microscope with a fitted charge coupled device camera was used to monitor the Li plating/stripping processes in real-time.

Electrochemical Measurements. To evaluate Li plating/stripping stability, the Li||Li symmetric batteries were assembled with two identical Li metal (bare Li or *o*-carborane/Li) electrodes, a Celgard 2500 separator, and 40 μL conventional carbonate-based or ether-based electrolytes. The conventional carbonate-based electrolyte is 1.0 M lithium hexafluorophosphate ($LiPF_6$) dissolved in ethylene carbonate/dimethyl carbonate/ethyl methyl carbonate (EC/DMC/EMC, volume ratio of 1:1:1) cosolvents with 1.0 wt % vinylene carbonate (VC) as additive. The conventional ether-based electrolyte is 1.0 M lithium bis(trifluoromethylsulfonyl)imide (LiTFSI) dissolve in 1,2-dimethoxyethane/1,3-dioxolane (DME/DOL, volume ratio of

https://doi.org/10.1021/acsnano.5c14816
ACS Nano 2025, 19, 38760−38772

1:1) cosolvents with 1.0 wt % lithium nitrate ($LiNO_3$) as additive. Electrochemical impedance spectra (EIS) tests of Li||Li symmetric batteries were carried out in a frequency range from 100 kHz to 100 mHz. Tafel plots of Li||Li symmetric batteries were tested at a scan rate of 5.0 mV s^{-1} from −0.2 to 0.2 V for calculating exchange current density values (i_0). To estimate the Li plating/stripping reversibility, the Li||Cu half batteries were assembled to measure the average Coulombic efficiency (CE). The average CE over n cycles can be calculated according to eq 1

$$CE_{avg} = \frac{\left[Q_c - \frac{(XQ_l - Q_r)}{N}\right]}{Q_c} \times 100\% \quad (1)$$

where N is the number of cycles, Q_c is the fixed plating or striping capacity involved in a single plating or stripping process (half cycle), Q_l is the initial Li plating capacity, and Q_r is the capacity retention measured in the final Li stripping process.

Cyclic voltammetry (CV) curves of Li||Cu half batteries were measured at a scan rate of 5.0 mV s^{-1} from 0.8 to −0.4 V. Linear sweep voltammetry (LSV) measurements were conducted based on Li||carbon-coated Al foil half batteries at a scan rate of 0.5 mV s^{-1}. The electrolyte used for the Li||LFP and Li||NCM811 batteries was the conventional carbonate-based electrolyte. The voltage windows for testing the Li||LFP and Li||NCM811 batteries were 2.6−4.2 V and 2.8−4.4 V, respectively. All batteries were galvanostatically cycled on a LAND-CT2001 8-channel battery tester. All other electrochemical tests mentioned above were performed on a Chenhua CHI-760 electrochemical workstation.

Theoretical Calculations. All density functional theory (DFT) calculations were performed with the Gaussian 16 software package. The Frontier molecular orbital energies and geometry optimization of $(CH_2OCO_2Li)_2$, CH_3OCO_2Li, Li_2CO_3, Li_2O, LiF, LiOH and *o*-carborane were calculated at B3LYP/6-31G(d,p) level. The electrostatic potential (ESP) and charge distribution of *o*-carborane were obtained by the embedded program inside Gaussian.

ASSOCIATED CONTENT

Supporting Information

The Supporting Information is available free of charge at https://pubs.acs.org/doi/10.1021/acsnano.5c14816.

Stability tests of *o*-carborane in THF solution; theoretical calculations of *o*-carborane molecule; characterizations (SEM, EDX, Raman, XPS, and Operando optical microscopy) and ambient atmosphere stability tests of the cycled *o*-carborane/Li electrodes; electrochemical measurements of batteries; characterizations (SEM and EDX) of the cycled LFP cathodes; summary tables of Frontier molecular orbital energies and electrochemical performances (PDF)

AUTHOR INFORMATION

Corresponding Author

Zhong Jin − *State Key Laboratory of Coordination Chemistry, MOE Key Laboratory of Mesoscopic Chemistry, MOE Key Laboratory of High Performance Polymer Materials and Technology, Jiangsu Key Laboratory of Clean Energy Catalysis and Intelligent Green Chemical Engineering, Suzhou Key Laboratory of Green Intelligent Manufacturing of New Energy Materials and Devices, Tianchang New Materials and Energy Technologies Research Center, Institute of Green Chemistry and Engineering, School of Chemistry and Chemical Engineering, Nanjing University, Nanjing, Jiangsu 210023, P. R. China;* orcid.org/0000-0001-8860-8579; Email: zhongjin@nju.edu.cn

Authors

Yaoda Wang − *State Key Laboratory of Coordination Chemistry, MOE Key Laboratory of Mesoscopic Chemistry, MOE Key Laboratory of High Performance Polymer Materials and Technology, Jiangsu Key Laboratory of Clean Energy Catalysis and Intelligent Green Chemical Engineering, Suzhou Key Laboratory of Green Intelligent Manufacturing of New Energy Materials and Devices, Tianchang New Materials and Energy Technologies Research Center, Institute of Green Chemistry and Engineering, School of Chemistry and Chemical Engineering, Nanjing University, Nanjing, Jiangsu 210023, P. R. China*

Junchuan Liang − *State Key Laboratory of Coordination Chemistry, MOE Key Laboratory of Mesoscopic Chemistry, MOE Key Laboratory of High Performance Polymer Materials and Technology, Jiangsu Key Laboratory of Clean Energy Catalysis and Intelligent Green Chemical Engineering, Suzhou Key Laboratory of Green Intelligent Manufacturing of New Energy Materials and Devices, Tianchang New Materials and Energy Technologies Research Center, Institute of Green Chemistry and Engineering, School of Chemistry and Chemical Engineering, Nanjing University, Nanjing, Jiangsu 210023, P. R. China*

Tianyu Shen − *State Key Laboratory of Coordination Chemistry, MOE Key Laboratory of Mesoscopic Chemistry, MOE Key Laboratory of High Performance Polymer Materials and Technology, Jiangsu Key Laboratory of Clean Energy Catalysis and Intelligent Green Chemical Engineering, Suzhou Key Laboratory of Green Intelligent Manufacturing of New Energy Materials and Devices, Tianchang New Materials and Energy Technologies Research Center, Institute of Green Chemistry and Engineering, School of Chemistry and Chemical Engineering, Nanjing University, Nanjing, Jiangsu 210023, P. R. China*

Xingkai Ma − *State Key Laboratory of Coordination Chemistry, MOE Key Laboratory of Mesoscopic Chemistry, MOE Key Laboratory of High Performance Polymer Materials and Technology, Jiangsu Key Laboratory of Clean Energy Catalysis and Intelligent Green Chemical Engineering, Suzhou Key Laboratory of Green Intelligent Manufacturing of New Energy Materials and Devices, Tianchang New Materials and Energy Technologies Research Center, Institute of Green Chemistry and Engineering, School of Chemistry and Chemical Engineering, Nanjing University, Nanjing, Jiangsu 210023, P. R. China*

Zuoxiu Tie − *State Key Laboratory of Coordination Chemistry, MOE Key Laboratory of Mesoscopic Chemistry, MOE Key Laboratory of High Performance Polymer Materials and Technology, Jiangsu Key Laboratory of Clean Energy Catalysis and Intelligent Green Chemical Engineering, Suzhou Key Laboratory of Green Intelligent Manufacturing of New Energy Materials and Devices, Tianchang New Materials and Energy Technologies Research Center, Institute of Green Chemistry and Engineering, School of Chemistry and Chemical Engineering, Nanjing University, Nanjing, Jiangsu 210023, P. R. China*

Complete contact information is available at: https://pubs.acs.org/10.1021/acsnano.5c14816

Author Contributions

The manuscript was written through contributions of all authors. All authors have given approval to the final version of the manuscript.

https://doi.org/10.1021/acsnano.5c14816
ACS Nano 2025, 19, 38760−38772

Notes

The authors declare no competing financial interest.

ACKNOWLEDGMENTS

The authors appreciate the supports from the National Natural Science Foundation of China (22561160129, 22479074, 22475096), the Equipment Pre-Research and Ministry of Education Joint Fund (8091B02052407), the Fundamental Research Program Key Project of Jiangsu Province (BK20253008), the Science and Technology Major Project of Jiangsu Province (BG2024013), the Natural Science Foundation of Jiangsu Province (BK20240400, BK20241236), the Scientific and Technological Achievements Transformation Special Fund of Jiangsu Province (BA2023037), the Academic Degree and Postgraduate Education Reforming Project of Jiangsu Province (JGKT24_C001), the Key Core Technology Open Competition Project of Suzhou City (SYG2024122), the Open Research Fund of Suzhou Laboratory (SZLAB-1308-2024-TS005), and the Chenzhou National Sustainable Development Agenda Innovation Demonstration Zone Provincial Special Project (2023sfq11).

REFERENCES

(1) Cheng, X. B.; Zhang, R.; Zhao, C. Z.; Zhang, Q. Toward Safe Lithium Metal Anode in Rechargeable Batteries: A Review. *Chem. Rev.* **2017**, *117*, 10403−10473.
(2) Bai, P.; Li, J.; Brushett, F. R.; Bazant, M. Z. Transition of Lithium Growth Mechanisms in Liquid Electrolytes. *Energy Environ. Sci.* **2016**, *9*, 3221−3229.
(3) Lin, D. C.; Liu, Y. Y.; Cui, Y. Reviving the Lithium Metal Anode for High-Energy Batteries. *Nat. Nanotechnol.* **2017**, *12*, 194−206.
(4) Lu, Y.; Tu, Z.; Archer, L. A. Stable Lithium Electrodeposition in Liquid and Nanoporous Solid Electrolytes. *Nat. Mater.* **2014**, *13*, 961−969.
(5) Tikekar, M. D.; Choudhury, S.; Tu, Z. Y.; Archer, L. A. Design Principles for Electrolytes and Interfaces for Stable Lithium-Metal Batteries. *Nat. Energy* **2016**, *1*, 16114.
(6) Xu, W.; Wang, J. L.; Ding, F.; Chen, X. L.; Nasybulin, E.; Zhang, Y. H.; Zhang, J. G. Lithium Metal Anodes for Rechargeable Batteries. *Energy Environ. Sci.* **2014**, *7*, 513−537.
(7) Cao, R.; Xu, W.; Lv, D.; Xiao, J.; Zhang, J. G. Anodes for Rechargeable Lithium-Sulfur Batteries. *Adv. Energy Mater.* **2015**, *5*, 1402273.
(8) Yin, Y. C.; Wang, Q.; Yang, J. T.; Li, F.; Zhang, G. Z.; Jiang, C. H.; Mo, H. S.; Yao, J. S.; Wang, K. H.; Zhou, F.; Ju, H. X.; Yao, H. B. Metal Chloride Perovskite Thin Film Based Interfacial Layer for Shielding Lithium Metal from Liquid Electrolyte. *Nat. Commun.* **2020**, *11*, 1761.
(9) Zheng, G. Y.; Lee, S. W.; Liang, Z.; Lee, H. W.; Yan, K.; Yao, H. B.; Wang, H. T.; Li, W. Y.; Chu, S.; Cui, Y. Interconnected Hollow Carbon Nanospheres for Stable Lithium Metal Anodes. *Nat. Nanotechnol.* **2014**, *9*, 618−623.
(10) Liang, X.; Pang, Q.; Kochetkov, I. R.; Sempere, M. S.; Huang, H.; Sun, X. Q.; Nazar, L. F. A Facile Surface Chemistry Route to a Stabilized Lithium Metal Anode. *Nat. Energy* **2017**, *2*, 17119.
(11) Niu, C. J.; Pan, H. L.; Xu, W.; Xiao, J.; Zhang, J. G.; Luo, L.; Wang, C.; Mei, D.; Meng, J.; Wang, X.; Liu, Z.; Mai, L.; et al. Self-Smoothing Anode for Achieving High-Energy Lithium Metal Batteries under Realistic Conditions. *Nat. Nanotechnol.* **2019**, *14*, 594−601.
(12) Xia, Y. C.; Zhou, P.; Kong, X.; Tian, J. K.; Zhang, W. L.; Yan, S. S.; Hou, W.-H.; Zhou, H.-Y.; Dong, H.; Chen, X. X.; Wang, P. C.; Xu, Z. A.; Wan, L.; Wang, B. G.; Liu, K. Designing an Asymmetric Ether-Like Lithium Salt to Enable Fast-Cycling High-Energy Lithium Metal Batteries. *Nat. Energy* **2023**, *8*, 934−945.
(13) Zhou, P.; Zhou, H. Y.; Xia, Y. C.; Feng, Q. Q.; Kong, X.; Hou, W.-H.; Ou, Y.; Song, X.; Zhou, H.-Y.; Zhang, W. L.; Lu, Y.; Liu, F. X.; Cao, Q. B.; Liu, H.; Yan, S. S.; Liu, K. Rational Lithium Salt Molecule Tuning for Fast Charging/Discharging Lithium Metal Battery. *Angew. Chem., Int. Ed.* **2024**, *63*, No. e202316717.
(14) Zhao, Z. F.; Wang, A. X.; Chen, A.; Zhao, Y. M.; Hu, Z. L.; Wu, K.; Luo, J. Y. Leveraging Ion Pairing and Transport in Localized High-Concentration Electrolytes for Reversible Lithium Metal Anodes at Low Temperatures. *Angew. Chem., Int. Ed.* **2024**, *63*, No. e202412239.
(15) Jin, S.; Jiang, Y.; Ji, H. X.; Yu, Y. Advanced 3D Current Collectors for Lithium-Based Batteries. *Adv. Mater.* **2018**, *30*, 1802014.
(16) Park, S.; Jin, H. J.; Yun, Y. S. Advances in the Design of 3D-Structured Electrode Materials for Lithium-Metal Anodes. *Adv. Mater.* **2020**, *32*, 2002193.
(17) Lin, H. N.; Zhang, Z. W.; Wang, Y. D.; Zhang, X. L.; Tie, Z. X.; Jin, Z. Template-Sacrificed Hot Fusion Construction and Nanoseed Modification of 3D Porous Copper Nanoscaffold Host for Stable-Cycling Lithium Metal Anodes. *Adv. Funct. Mater.* **2021**, *31*, 2102735.
(18) Zhou, F.; Li, Z.; Lu, Y.-Y.; Shen, B.; Guan, Y.; Wang, X.-X.; Yin, Y.-C.; Zhu, B.-S.; Lu, L.-L.; Ni, Y.; Cui, Y.; Yao, H.-B.; Yu, S.-H. Diatomite Derived Hierarchical Hybrid Anode for High Performance All-Solid-State Lithium Metal Batteries. *Nat. Commun.* **2019**, *10*, 2482.
(19) Wang, C. W.; Fu, K.; Kammampata, S. P.; McOwen, D. W.; Samson, A. J.; Zhang, L.; Hitz, G. T.; Nolan, A. M.; Wachsman, E. D.; Mo, Y. F.; Thangadurai, V.; Hu, L. B. Garnet-Type Solid-State Electrolytes: Materials, Interfaces, and Batteries. *Chem. Rev.* **2020**, *120*, 4257−4300.
(20) Liang, J. Y.; Zeng, X. X.; Zhang, X. D.; Zuo, T. T.; Yan, M.; Yin, Y. X.; Shi, J. L.; Wu, X. W.; Guo, Y. G.; Wan, L. J. Engineering Janus Interfaces of Ceramic Electrolyte via Distinct Functional Polymers for Stable High-Voltage Li-Metal Batteries. *J. Am. Chem. Soc.* **2019**, *141*, 9165−9169.
(21) Wang, Z. J.; Wang, Y. Y.; Wu, C.; Pang, W. K.; Mao, J. F.; Guo, Z. P. Constructing Nitrided Interfaces for Stabilizing Li Metal Electrodes in Liquid Electrolytes. *Chem. Sci.* **2021**, *12*, 8945−8966.
(22) Ju, Z. J.; Nai, J.; Wang, Y.; Liu, T. F.; Zheng, J. H.; Yuan, H. D.; Sheng, O. W.; Jin, C. B.; Zhang, W. K.; Jin, Z.; Tian, H.; Liu, Y. J.; Tao, X. Y. Biomacromolecules Enabled Dendrite-Free Lithium Metal Battery and its Origin Revealed by Cryoelectron Microscopy. *Nat. Commun.* **2020**, *11*, 488.
(23) Hu, A. J.; Chen, W.; Du, X. C.; Hu, Y.; Lei, T. Y.; Wang, H. B.; Xue, L. X.; Li, Y. Y.; Sun, H.; Yan, Y. C.; Long, J. P.; Shu, C. Z.; Zhu, J.; Li, B.; Wang, X.; et al. An artificial hybrid interphase for an ultrahigh-rate and practical lithium metal anode. *Energy Environ. Sci.* **2021**, *14*, 4115−4124.
(24) Chen, T.; Meng, F. B.; Zhang, Z. W.; Liang, J. C.; Hu, Y.; Kong, W. H.; Zhang, X. L.; Jin, Z. Stabilizing Lithium Metal Anode by Molecular Beam Epitaxy Grown Uniform and Ultrathin Bismuth Film. *Nano Energy* **2020**, *76*, 105068.
(25) Yu, Z. A.; Cui, Y.; Bao, Z. N. Design Principles of Artificial Solid Electrolyte Interphases for Lithium-Metal Anodes. *Cell Rep. Phys. Sci.* **2020**, *1*, 100119.
(26) Wang, Y. D.; Liang, J. C.; Song, X. M.; Jin, Z. Recent Progress in Constructing Halogenated Interfaces for Highly Stable Lithium Metal Anodes. *Energy Storage Mater.* **2023**, *54*, 732−775.
(27) Xu, R.; Cheng, X.; Yan, C.; Zhang, X.; Xiao, Y.; Zhao, C.; Huang, J.; Zhang, Q. Artificial Interphases for Highly Stable Lithium Metal Anode. *Matter* **2019**, *1*, 317−344.
(28) Scholz, M.; Hey-Hawkins, E. Carbaboranes as Pharmacophores: Properties, Synthesis, and Application Strategies. *Chem. Rev.* **2011**, *111*, 7035−7062.
(29) Liu, S. M.; Chen, Z. J.; Zhang, Q. H.; Zhang, S. G.; Li, Z. P.; Shi, F.; Ma, X. Y.; Deng, Y. Q. Carborane-Derivatized Low-Melting Salts with Ether-Functionalized Cations − Preparation and Properties. *Eur. J. Inorg. Chem.* **2011**, *2011*, 1910−1920.

https://doi.org/10.1021/acsnano.5c14816
ACS Nano 2025, 19, 38760−38772

(30) Jotham, R. W.; Reynolds, D. J. The Vibrational Spectra of the Carboranes. Part I. The Small *closo*-Carboranes $C_2B_3H_5$, 1,6-$C_2B_4H_6$, and $C_2B_5H_7$. *J. Chem. Soc. Inorg. Phys. Theor.* **1971**, 3181−3191.
(31) Genisel, M. F.; Uddin, M. N.; Say, Z.; Kulakci, M.; Turan, R.; Gulseren, O.; Bengu, E. Bias in Bonding Behavior among Boron, Carbon, and Nitrogen Atoms in Ion Implanted a-BN, a-BC, and Diamond like Carbon Films. *J. Appl. Phys.* **2011**, *110*, 074906.
(32) Imam, M.; Höglund, C.; Jensen, J.; Schmidt, S.; Ivanov, I. G.; Hall-Wilton, R.; Birch, J.; Pedersen, H. Trimethylboron as Single-Source Precursor for Boron-Carbon Thin Film Synthesis by Plasma Chemical Vapor Deposition. *J. Phys. Chem. C* **2016**, *120*, 21990−21997.
(33) Zhang, W. D.; Zhang, S. Q.; Fan, L.; Gao, L. N.; Kong, X. Q.; Li, S. Y.; Li, J.; Hong, X.; Lu, Y. Y. Tuning the LUMO Energy of an Organic Interphase to Stabilize Lithium Metal Batteries. *ACS Energy Lett.* **2019**, *4*, 644−650.
(34) Goodenough, J. B.; Kim, Y. Challenges for Rechargeable Li Batteries. *Chem. Mater.* **2010**, *22*, 587−603.
(35) Wu, J. Y.; Rao, Z. X.; Liu, X. T.; Shen, Y.; Fang, C.; Yuan, L. X.; Li, Z.; Zhang, W. X.; Xie, X. L.; Huang, Y. H. Polycationic Polymer Layer for Air-Stable and Dendrite-Free Li Metal Anodes in Carbonate Electrolytes. *Adv. Mater.* **2021**, *33*, 2007428.
(36) Shen, X.; Li, Y.; Qian, T.; Liu, J.; Zhou, J.; Yan, C.; Goodenough, J. B. Lithium Anode Stable in Air for Low-Cost Fabrication of a Dendrite-Free Lithium Battery. *Nat. Commun.* **2019**, *10*, 900.
(37) Chen, T.; Kong, W.; Zhao, P.; Lin, H.; Hu, Y.; Chen, R.; Yan, W.; Jin, Z. Dendrite-Free and Stable Lithium Metal Anodes Enabled by an Antimony-Based Lithiophilic Interphase. *Chem. Mater.* **2019**, *31*, 7565−7573.
(38) Gao, R.-M.; Yang, H.; Wang, C.-Y.; Ye, H.; Cao, F.-F.; Guo, Z.-P. Fatigue-Resistant Interfacial Layer for Safe Lithium Metal Batteries. *Angew. Chem., Int. Ed.* **2021**, *60*, 25508−25513.
(39) Adair, K. R.; Zhao, C.; Banis, M. N.; Zhao, Y.; Li, R.; Cai, M.; Sun, X. Highly Stable Lithium Metal Anode Interface via Molecular Layer Deposition Zircone Coatings for Long Life Next-Generation Battery Systems. *Angew. Chem., Int. Ed.* **2019**, *58*, 15797−15802.
(40) Liu, F.; Xiao, Q.; Wu, H. B.; Shen, L.; Xu, D.; Cai, M.; Lu, Y. Fabrication of Hybrid Silicate Coatings by a Simple Vapor Deposition Method for Lithium Metal Anodes. *Adv. Energy Mater.* **2018**, *8*, 1701744.
(41) Cui, Y.; Liu, S.; Wang, D.; Wang, X.; Xia, X.; Gu, C.; Tu, J. A Facile Way to Construct Stable and Ionic Conductive Lithium Sulfide Nanoparticles Composed Solid Electrolyte Interphase on Li Metal Anode. *Adv. Funct. Mater.* **2021**, *31*, 2006380.
(42) Chen, D.; Huang, S.; Zhong, L.; Wang, S.; Xiao, M.; Han, D.; Meng, Y. In Situ Preparation of Thin and Rigid COF Film on Li Anode as Artificial Solid Electrolyte Interphase Layer Resisting Li Dendrite Puncture. *Adv. Funct. Mater.* **2020**, *30*, 1907717.
(43) Luo, J.; Huang, Q.; Shi, D.; Qiu, Y.; Zheng, X.; Yang, S.; Li, B.; Weng, J.; Wu, M.; Liu, Z.; Yu, Y.; Yang, C. Dynamic Interfacial Protection via Molecularly Tailored Copolymer for Durable Artificial Solid Electrolyte Interphase in Lithium Metal Batteries. *Adv. Funct. Mater.* **2024**, *34*, 2403021.
(44) Huang, H.; Liu, S.; Xie, Y.; Liu, J.; Shi, C.; Sun, M.; Peng, H.; Lan, J.; Deng, Y.-P.; Huang, L.; Sun, S.-G. Constructing an Artificial Interface as a Bifunctional Promoter for the Li Anode and the NCM Cathode in Lithium Metal Batteries. *J. Am. Chem. Soc.* **2024**, *146*, 31137−31149.
(45) Li, K.; Wang, Z.; Yang, B.; Li, T.; Li, B.; Chen, J.; Yan, Z.; He, M.; Hu, A.; Long, J. Elucidating the Role of Polar Functional Groups in Fluorinated Polymer Artificial Interphase for Stable Lithium Anodes. *Chem. Eng. J.* **2024**, *493*, 152527.
(46) Meng, J. W.; Chu, F. L.; Hu, J. L.; Li, C. L. Liquid Polydimethylsiloxane Grafting to Enable Dendrite-Free Li Plating for Highly Reversible Li-Metal Batteries. *Adv. Funct. Mater.* **2019**, *29*, 1902220.
(47) Zheng, J. M.; Engelhard, M. H.; Mei, D. H.; Jiao, S. H.; Polzin, B. J.; Zhang, J. G.; Xu, W. Electrolyte Additive Enabled Fast Charging and Stable Cycling Lithium Metal Batteries. *Nat. Energy* **2017**, *2*, 17012.
(48) Yan, C.; Yao, Y. X.; Chen, X.; Cheng, X. B.; Zhang, X. Q.; Huang, J. Q.; Zhang, Q. Lithium Nitrate Solvation Chemistry in Carbonate Electrolyte Sustains High-Voltage Lithium Metal Batteries. *Angew. Chem., Int. Ed.* **2018**, *57*, 14055−14059.
(49) Jie, Y. L.; Liu, X. J.; Lei, Z. W.; Wang, S. Y.; Chen, Y. W.; Huang, F. Y.; Cao, R. G.; Zhang, G. Q.; Jiao, S. H. Enabling High-Voltage Lithium Metal Batteries by Manipulating Solvation Structure in Ester Electrolyte. *Angew. Chem., Int. Ed.* **2020**, *59*, 3505−3510.
(50) Wang, R.; Wang, L.; Liu, R.; Li, X. Y.; Wu, Y. Z.; Ran, F. "Fast-Charging" Anode Materials for Lithium-Ion Batteries from Perspective of Ion Diffusion in Crystal Structure. *ACS Nano* **2024**, *18*, 2611−2648.

https://doi.org/10.1021/acsnano.5c14816
ACS Nano 2025, 19, 38760−38772